Orbital Angular Momentum Modes from VCSELs using Grayscale Photolithography

Raman Kumar, *Student Member, IEEE,* Pawel Strzebonski, *Student Member, IEEE,* Katherine Lakomy, *Student Member, IEEE,* Kent D. Choquette, *Fellow, IEEE*

***Abstract*—We present fabrication of dielectric micro-optical elements on VCSELs and characterization of emitted orbital angular momentum modes. Spiral phase plates are fabricated on the top facet of oxide-confined VCSELs using grayscale photolithography and dry etching silicon nitride. The refractive index of silicon nitride film is characterized using ellipsometry and atomic force microscopy is used to verify the fidelity of fabricated dielectric micro-optical elements. Orbital angular momentum modes with on-axis null are experimentally demonstrated. A novel circular rotation of intensity with propagation in the near-field is observed and is analyzed using Fresnel transfer function simulations.**

***Index Terms*—Orbital Angular Momentum Modes, VCSELs, Grayscale Photolithography, Integrated Spiral Phase Plates**

I. Introduction

ORBITAL angular momentum (OAM) modes have the potential of increasing data transmission capacity of optical links [1]. OAM modes are characterized by helical phase front and the twist of helix is defined by a topological charge. In principle, infinite quantized OAM modes can be generated by varying the twisting rate of the helix and all such modes form an orthogonal basis set. This orthogonality leads to minimal inter-modal crosstalk and allows the OAM modes to be employed in space-division multiplexing. Various techniques to generate OAM modes have been explored such as spiral plates [2, 3] and metamaterials [4, 5]. Vertical cavity surface emitting lasers (VCSELs) have been shown to naturally emit vortex-like optical modes [6]. Engineered OAM mode generation from vertical cavity surface emitting lasers (VCSELs) offers unique advantages such as 2-dimensional arrays and high-speed data modulation bandwidth [7, 8]. Further, the vertical emission is naturally suited for integration of micro-optical elements on top facet to engineer the natural Gaussian family of modes into other modes with desired properties, such as OAM modes. A VCSEL emitting an OAM mode has the potential to add space-division multiplexing component to high-speed temporal operation for increased transmission bandwidth. Previously, an integrated spiral plate was etched into a silicon nitride layer on the top facet using a focused ion-beam to generate OAM modes [3, 9]. But a serial ion-etching approach cannot be readily integrated into high-volume manufacturing and is likely to result in ion-induced physical etch damage. Other approaches to generate OAM modes including metasurfaces [10, 11] and Bragg-reflector waveguides [12] have also been explored. But complex fabrication requirements may inhibit their scalability.

In this letter, we present a novel process for fabricating complex dielectric microstructures; herein we consider an integrated spiral plate on top of a nominally 850nm VCSEL fabricated using grayscale photolithography. Grayscale photolithography uses power modulation of a scanning UV laser to expose different depths in a positive photoresist [13]. An integrated spiral plate with 8-levels is sculpted in photoresist and then transferred into a silicon nitride (SiNx) film by dry etching with 1:1 selectivity. Oxide-confined VCSELs are subsequently fabricated demonstrating the fabrication process is readily integrable with conventional VCSEL manufacturing. OAM modes with on-axis intensity null are demonstrated. A novel rotating intensity pattern is observed with propagation of these modes in the near-field and is explained using propagation simulations.

II. Device Design and Fabrication

The complete fabrication process is illustrated in Fig. 1 and shows the micro-optical elements are fabricated first followed by conventional VCSEL fabrication [14]. The VCSEL epitaxy used in this work has a three quantum well active region designed for 850nm wavelength emission with 22 periods in the upper p-type DBR mirror and a lower 34 period n-type DBR mirror. After top p-type Ti/Au ring contacts and broad area bottom AuGe/Ni/Au contacts are deposited, a 1μm thick low-stress SiNx film is subsequently deposited using mixed-frequency STS plasma enhanced chemical vapor deposition system. The refractive index of the SiNx film is measured at 850nm using variable angle ellipsometry measurements to be 1.939. Based on this refractive index, the required step for a spiral plate in SiNx with a topological charge of +1 is

$$h = \frac{\lambda_0}{n_{SiNx} - n_{air}} \qquad (1)$$

The authors are affiliated with the Department of Electrical and Computer Engineering, University of Illinois at Urbana-Champaign, Urbana, IL, USA, 61801. (email: ramank2@illinois.edu; strzebo2@illinois.edu; lakomy2@illinois.edu; choquett@illinois.edu).

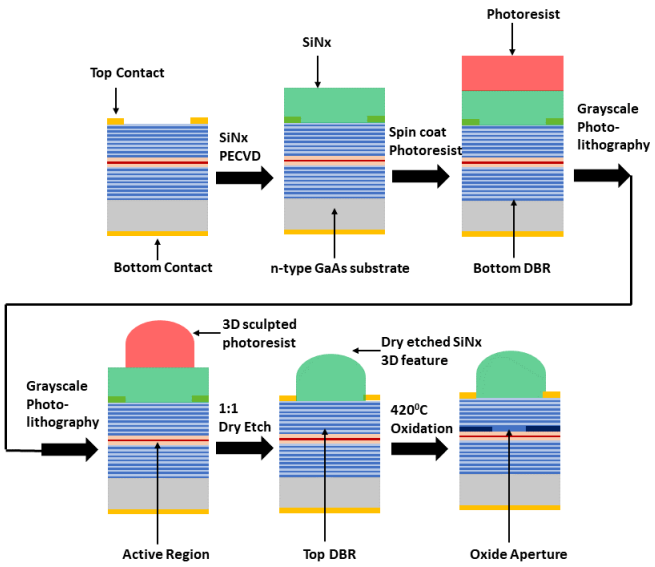

Fig. 1 Fabrication process flowchart for oxide confined VCSELs with integrated spiral plate

Here, λ_0 is the free space wavelength equal to 850nm, n_{SiNx} is the measured refractive index of SiNx film and n_{air} is assumed to be 1. The maximum silicon nitride thickness is 905.2nm, so for an 8-step spiral each step height is 113.1nm. A positive photoresist AZ5214 is spin coated to a thickness of 2.15µm. To define a 3-dimensional (3D) pattern in photoresist, a scanning UV laser system manufactured by Heidelberg Instruments is used [15]. A grayscale contrast curve is generated as shown in Fig. 2(a) to calibrate the process recipe for required photoresist exposure levels to sculpt 3D features.

Multiple 8-level spiral plates with diameter of 20µm are patterned in photoresist by using the contrast curve shown in Fig. 2(a). The 3D sculpted PR pattern is then transferred to the

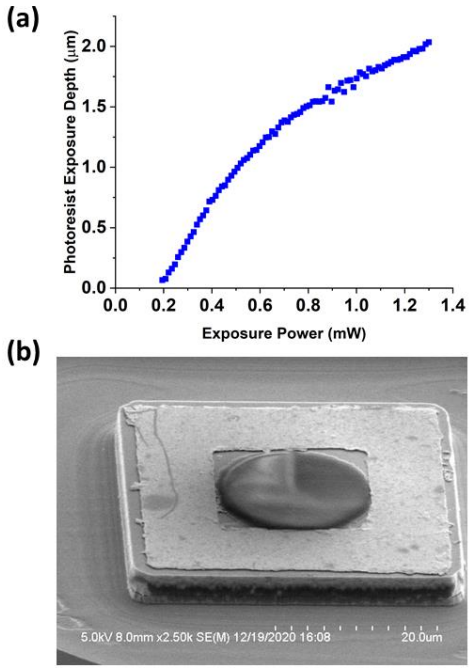

Fig. 2 (a) PR contrast curve for grayscale photolithography (b) SEM image for Spiral VCSEL A

SiNx film by dry etching with an etch selectivity of 1:1. The dry etch was done using Oxford Instruments PlasmaPro100 system with the recipe: RF/ICP Power = 50/0W; SF_6 flow rate = 15sccm; Chamber Pressure = 3mTorr and Table Temperature = 5^0C. After fabrication of dielectric micro-optical elements, we next fabricate mesa defined oxide-confined VCSELs [14]. Two single mode VCSELs with approximate oxide apertures of 4µmx4µm and 10µmx10µm are characterized next and are henceforth named Spiral VCSEL A and Spiral VCSEL B, respectively. A scanning electron micrograph (SEM) image of Spiral VCSEL A in Fig. 2(b) shows the feasibility of fabricating spirals on top of the VCSEL mesa with precise alignment.

III. RESULTS AND DISCUSSION

Structural characterization on spiral VCSELs is performed using an Anton Paar Tosca atomic force microscope (AFM). The three-dimensional AFM image and false color step height for Spiral VCSEL B are shown in Fig. 3(a) and Fig. 3(b),

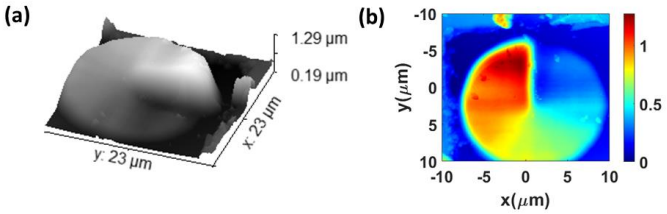

Fig. 3 (a)3D view of AFM image for Spiral VCSEL B (b) Flat view of AFM image for Spiral VCSEL B with color bar showing range of step height in microns

respectively. The AFM scan covers an area of approximately 20µmx20µm with a lateral and vertical resolution of 50nm. The high fidelity of the fabricated spirals confirmed in Fig. 3, is used in subsequent optical propagation simulations.

The false color height data (e.g. Fig. 3(b)) confirm the required step height for spiral plate. The micro-optical element in Spiral VCSEL B, in Fig. 3(b) shows a maximum and minimum step height of 1.0564µm and 0.2341µm respectively, with a step height difference of 0.8223µm. The fabricated step height difference between maximum and minimum is very close to ideal value of 0.792µm.

Electrical and optical characterization on spiral VCSELs is then performed. The output power versus current characteristics of Spiral VCSEL A and Spiral VCSEL B are compared to their respective control VCSELs without a spiral plate on their top facet in Fig. 4(a) and Fig. 4(b) respectively. An increase in threshold and reduction in differential quantum efficiency is observed for spiral VCSELs in comparison to the control VCSELs. This can be attributed to increase in scattering loss at the top DBR due to the presence of spiral plates. The optical spectra for the spiral VCSELs are shown in Fig. 4(c) and Fig. 4(d). The small oxide-aperture Spiral VCSEL A in Fig. 4(c) emits a single Gaussian mode at 1.4mA. The broad-area oxide Spiral VCSEL B also emits into an approximately single, albeit higher order mode [16] with other modes suppressed by 10dB in Fig. 4(d). A top-view optical microscope image of Spiral VCSEL A is shown in Fig. 5(a) at 1.4mA. The dotted circle shows the extent of spiral plate and the center region outlines

This article has been accepted for publication in a future issue of this journal, but has not been fully edited. Content may change prior to final publication. Citation information: DOI 10.1109/LPT.2021.3075891, IEEE Photonics Technology Letters

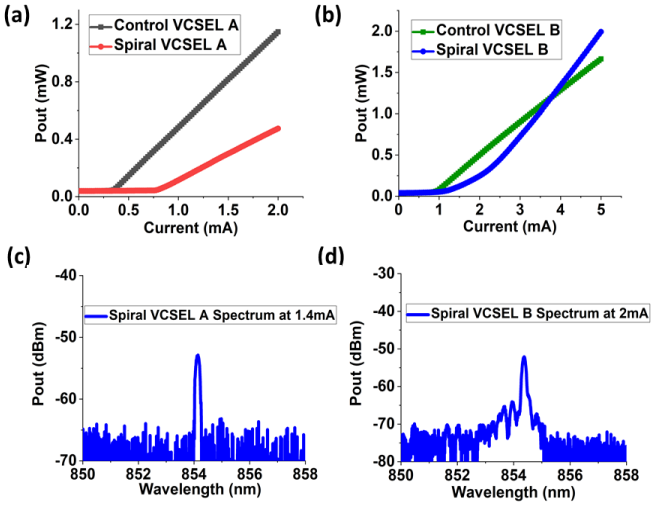

Fig. 4 (a), (b) LI comparison of spiral VCSELs with control VCSELs of similar aperture (c) Optical spectrum of Spiral VCSEL A at 1.4mA (d) Optical spectrum of Spiral VCSEL B at 2mA

the oxide aperture. The near-field intensity profile exhibits an obvious intensity null in the center which is expected of an OAM mode [3, 6, 9]. A magnified near-field mode profile is shown in inset of Fig. 5(a). Given the near-field null is expected at the center of the spiral plate, the images in Fig. 5(a) shows the excellent alignment of the spiral plate into the center of the oxide aperture. Fig. 5(b) shows the experimentally measured far-field profile which exhibits on-axis intensity null. A simulated far-field intensity profile is shown in Fig. 5(c). To generate Fig. 5(c), surface height data from AFM measurements are transformed into a phase profile, with the height-to-phase adjusted until the phase change around the SPP is 2π radians. A Gaussian mode with 4μm width is aligned to the center of spiral plate and after propagation through the spiral plate, a complex near-field profile is generated. The near-field profile is then propagated using the Fresnel transfer function to obtain the far-field profile [17]. A qualitative match between Figs. 5(b) and 5(c) is found.

The near-field intensity profile of Spiral VCSEL B is further analyzed at an injection current of 2mA. An optical microscope

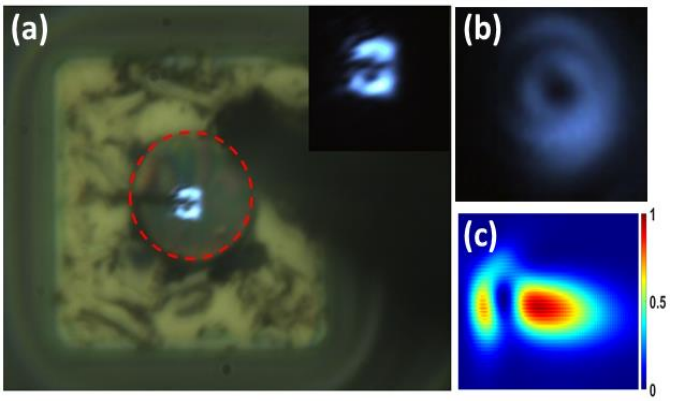

Fig. 5 (a) Optical microscope image of Spiral VCSEL A at 1.4mA. Red dotted circle shows extent of spiral and inset shows near-field mode profile. (b) Experimentally measured far-field intensity profile (c) Far-field intensity profile simulated by Fresnel transfer function. Color bar shows range of normalized intensity values

is used to capture a series of intensity profile images as the microscope focal plane is moved in the direction of beam propagation i.e., z-direction, approximately in the near-field. Since the emission from this large aperture VCSEL is dominated by a higher order mode (see Fig. 4(d)), multiple intensity spots are expected and observed as shown in Fig. 6(a). Figs. 6(a-f) shows the measured intensity evolution approximately in the near-field evolving to the far-field.

Starting from multiple spatial intensity lobes in Fig. 6(a), the mode transformation by the spiral is evident in Fig. 6(f) with

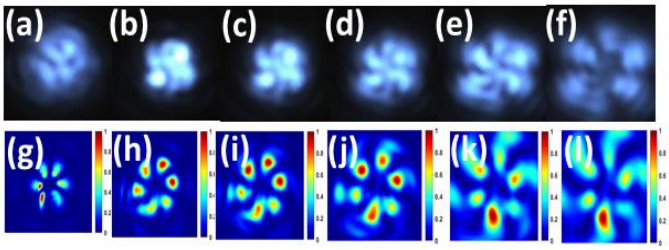

Fig. 6 (a-f) OAM mode evolution for Spiral VCSEL B at 2mA with increase in z from left to right (g-l) Fresnel transfer function simulation with increase in z from left to right

high intensity lobes radially separated from the center which has reduced intensity. As the microscope focal plane is moved in the z-direction, a clear rotation of intensity profile around the axis is observed. For comparison to the experimental results, a 6-lobed intensity distribution is assumed as shown in Fig. 6(g). Similar multi-lobed near-field intensity patterns from broad area VCSELs emitting into a single higher order mode have been previously reported [16]. The surface-height data from the AFM scan is again used in the Fresnel transfer function simulations where the calculated near-field profile is propagated in the near field at various distances to observe the spiral plate engineered mode. The alignment of the presumed mode profile, phase profile and height-to-phase mapping are further tuned to obtain a qualitative match in propagation behavior between the experimental results and simulation. The simulated propagation intensity profiles are shown in Fig. 6(g) to Fig. 6(l). Qualitative match with experimental results is apparent in Fig. 6, although other combinations of OAM modes could also produce similar intensity patterns. Such rotating fields have been previously demonstrated using spiral-zone plates [18] and have been explained using superposition of two optical vortex beams [19-21]. Whereas vector vortex beams from VCSELs with frequency selective external feedback have been previously reported[22], to the best of our knowledge this is the first time such rotating fields have been experimentally observed from a VCSEL with an integrated spiral plate.

IV. CONCLUSION

In conclusion, we have demonstrated a novel process for fabrication of integrated dielectric micro-optical elements, such as spiral phase plates with oxide-confined VCSELs. This integrated process can be used in high-volume manufacturing to generate OAM modes from VCSELs. The fidelity of fabricated structures is verified using SEM and AFM scans. A small threshold current and slope efficiency penalty is found owing to scattering loss at the top facet of VCSEL. On-axis

intensity nulls are experimentally demonstrated in both the near-field and far-field and a novel axial intensity rotation phenomenon is observed in the direction of propagation. The modal intensity profiles are qualitatively matched to simulated results using Fresnel transfer function simulations with the measured micro-optical dimensions. This work opens up additional opportunities for fabrication of other lens, grating micro-optical structures for VCSEL mode control and engineering.

ACKNOWLEDGMENT

The authors acknowledge the research staff and resources of Holonyak Micro and Nanotechnology Laboratory and the Frederick Seitz Materials Research Laboratory Central Research Facilities, both at University of Illinois.

REFERENCES

[1] A. E. Willner *et al.*, "Optical communications using orbital angular momentum beams," *Advances in Optics and Photonics*, vol. 7, no. 1, pp. 66-106, 2015.

[2] S. Oemrawsingh, J. Van Houwelingen, E. Eliel, J. Woerdman, E. Verstegen, and J. Kloosterboer, "Production and characterization of spiral phase plates for optical wavelengths," *Applied optics*, vol. 43, no. 3, pp. 688-694, 2004.

[3] H. Li *et al.*, "Orbital angular momentum vertical-cavity surface-emitting lasers," *Optica*, vol. 2, no. 6, pp. 547-552, 2015.

[4] N. Yu *et al.*, "Light propagation with phase discontinuities: generalized laws of reflection and refraction," *science*, vol. 334, no. 6054, pp. 333-337, 2011.

[5] M. S. Seghilani *et al.*, "Vortex Laser based on III-V semiconductor metasurface: direct generation of coherent Laguerre-Gauss modes carrying controlled orbital angular momentum," *Scientific reports*, vol. 6, no. 1, pp. 1-12, 2016.

[6] J. Scheuer and M. Orenstein, "Optical vortices crystals: Spontaneous generation in nonlinear semiconductor microcavities," *Science*, vol. 285, no. 5425, pp. 230-233, 1999.

[7] S. T. M. Fryslie, M. P. T. Siriani, D. F. Siriani, M. T. Johnson, and K. D. Choquette, "37-GHz modulation via resonance tuning in single-mode coherent vertical-cavity laser arrays," *IEEE Photonics Technology Letters*, vol. 27, no. 4, pp. 415-418, 2014.

[8] H. Dave *et al.*, "Digital Modulation of Coherently-Coupled 2x1 Vertical-Cavity Surface-Emitting Laser Arrays," *IEEE Photonics Technology Letters*, vol. 31, no. 2, pp. 173-176, 2018.

[9] P. Debernardi *et al.*, "Modal performance of spiral phase plate VCSELs," *IEEE Journal of Quantum Electronics*, vol. 52, no. 5, pp. 1-8, 2016.

[10] Y. Sun, J. Zhu, S. Liu, Y. Yu, and S. Yu, "Direct generation of orbital angular momentum beams by integrating all-dielectric metasurface to vertical-cavity surface-emitting laser," in *Asia Communications and Photonics Conference*, 2017: Optical Society of America, p. Su3K. 4.

[11] Y.-Y. Xie *et al.*, "Metasurface-integrated vertical cavity surface-emitting lasers for programmable directional lasing emissions," *Nature nanotechnology*, vol. 15, no. 2, pp. 125-130, 2020.

[12] K. Tanabe, X. Gu, A. Matsutni, and F. Koyama, "Compact vortex beam emitter laterally integrated with VCSEL array," in *2015 Conference on Lasers and Electro-Optics (CLEO)*, 2015: IEEE, pp. 1-2.

[13] A. Grushina, "Direct-write grayscale lithography," *Advanced Optical Technologies*, vol. 8, no. 3-4, pp. 163-169, 2019.

[14] K. D. Choquette and K. M. Geib, "Fabrication and performance of vertical-cavity surface-emitting lasers," *Vertical-cavity surfaceemitting lasers'(Cambridge University Press, New York, 1999)*, pp. 193-232, 1999.

[15] https://heidelberg-instruments.com/

[16] S. P. Hegarty, G. Huyet, J. G. McInerney, and K. Choquette, "Pattern formation in the transverse section of a laser with a large Fresnel number," *Physical Review Letters*, vol. 82, no. 7, p. 1434, 1999.

[17] D. Voelz, "Computational fourier optics: a MATLAB tutorial," 2011: Society of Photo-Optical Instrumentation Engineers.

[18] H. Liu *et al.*, "Twisted focusing of optical vortices with broadband flat spiral zone plates," *Advanced Optical Materials*, vol. 2, no. 12, pp. 1193-1198, 2014.

[19] D. Yang, J. Zhao, T. Zhao, and L. Kong, "Generation of rotating intensity blades by superposing optical vortex beams," *Optics Communications*, vol. 284, no. 14, pp. 3597-3600, 2011.

[20] S. Vyas, Y. Kozawa, and S. Sato, "Twisted longitudinally polarized field in the focal region," *Applied Physics B*, vol. 110, no. 1, pp. 7-14, 2013.

[21] Y. Liu, Z. Zhang, C. Li, D. Liu, and C. Kuang, "Rotating light fields of an azimuthally polarized light beam generated by two-belt spiral phase modulation," *Journal of Modern Optics*, vol. 65, no. 20, pp. 2295-2300, 2018.

[22] J. Jimenez-Garcia, P. Rodriguez, T. Guillet, and T. Ackemann, "Spontaneous formation of vector vortex beams in vertical-cavity surface-emitting lasers with feedback," *Physical review letters*, vol. 119, no. 11, p. 113902, 2017.